2021

Lysophospholipid acylation modulates plasma membrane lipid organization and insulin sensitivity in skeletal muscle

Patrick J Ferrara

Haowei Song

John Turk

et al

JCI The Journal of Clinical Investigation

Lysophospholipid acylation modulates plasma membrane lipid organization and insulin sensitivity in skeletal muscle

Patrick J. Ferrara, … , William L. Holland, Katsuhiko Funai

J Clin Invest. 2021;131(8):e135963. https://doi.org/10.1172/JCI135963.

Research Article | Metabolism | Muscle biology

Aberrant lipid metabolism promotes the development of skeletal muscle insulin resistance, but the exact identity of lipid-mediated mechanisms relevant to human obesity remains unclear. A comprehensive lipidomic analysis of primary myocytes from individuals who were insulin-sensitive and lean (LN) or insulin-resistant with obesity (OB) revealed several species of lysophospholipids (lyso-PLs) that were differentially abundant. These changes coincided with greater expression of lysophosphatidylcholine acyltransferase 3 (LPCAT3), an enzyme involved in phospholipid transacylation (Lands cycle). Strikingly, mice with skeletal muscle–specific knockout of LPCAT3 (LPCAT3-MKO) exhibited greater muscle lysophosphatidylcholine/phosphatidylcholine, concomitant with improved skeletal muscle insulin sensitivity. Conversely, skeletal muscle–specific overexpression of LPCAT3 (LPCAT3-MKI) promoted glucose intolerance. The absence of LPCAT3 reduced phospholipid packing of cellular membranes and increased plasma membrane lipid clustering, suggesting that LPCAT3 affects insulin receptor phosphorylation by modulating plasma membrane lipid organization. In conclusion, obesity accelerates the skeletal muscle Lands cycle, whose consequence might induce the disruption of plasma membrane organization that suppresses muscle insulin action.

Lysophospholipid acylation modulates plasma membrane lipid organization and insulin sensitivity in skeletal muscle

Patrick J. Ferrara,[1,2,3,4,5] Xin Rong,[6] J. Alan Maschek,[1,7] Anthony R.P. Verkerke,[1,2,3,4] Piyarat Siripoksup,[1,8] Haowei Song,[9] Thomas D. Green,[3] Karthickeyan C. Krishnan,[10] Jordan M. Johnson,[1,2,3,4] John Turk,[9] Joseph A. Houmard,[3,4] Aldons J. Lusis,[10] Micah J. Drummond,[1,5,8] Joseph M. McClung,[3] James E. Cox,[1,7,11] Saame Raza Shaikh,[3,12] Peter Tontonoz,[6] William L. Holland,[1,2,5] and Katsuhiko Funai[1,2,3,4,5,8]

[1]Diabetes and Metabolism Research Center and [2]Department of Nutrition and Integrative Physiology, University of Utah, Salt Lake City, Utah, USA. [3]East Carolina Diabetes and Obesity Institute and [4]Human Performance Laboratory, East Carolina University, Greenville, North Carolina, USA. [5]Molecular Medicine Program, University of Utah, Salt Lake City, Utah, USA. [6]Department of Pathology and Laboratory Medicine, UCLA, Los Angeles, California, USA. [7]Metabolomics, Mass Spectrometry, and Proteomics Core and [8]Department of Physical Therapy and Athletic Training, University of Utah, Salt Lake City, Utah, USA. [9]Division of Endocrinology Metabolism and Lipid Research, School of Medicine, Washington University in St. Louis, St. Louis, Missouri, USA. [10]Cardiology Division, Department of Medicine, UCLA, Los Angeles, California, USA. [11]Department of Biochemistry, University of Utah, Salt Lake City, Utah, USA. [12]Department of Nutrition, University of North Carolina at Chapel Hill, Chapel Hill, North Carolina, USA.

Aberrant lipid metabolism promotes the development of skeletal muscle insulin resistance, but the exact identity of lipid-mediated mechanisms relevant to human obesity remains unclear. A comprehensive lipidomic analysis of primary myocytes from individuals who were insulin-sensitive and lean (LN) or insulin-resistant with obesity (OB) revealed several species of lysophospholipids (lyso-PLs) that were differentially abundant. These changes coincided with greater expression of lysophosphatidylcholine acyltransferase 3 (LPCAT3), an enzyme involved in phospholipid transacylation (Lands cycle). Strikingly, mice with skeletal muscle–specific knockout of LPCAT3 (LPCAT3-MKO) exhibited greater muscle lysophosphatidylcholine/phosphatidylcholine, concomitant with improved skeletal muscle insulin sensitivity. Conversely, skeletal muscle–specific overexpression of LPCAT3 (LPCAT3-MKI) promoted glucose intolerance. The absence of LPCAT3 reduced phospholipid packing of cellular membranes and increased plasma membrane lipid clustering, suggesting that LPCAT3 affects insulin receptor phosphorylation by modulating plasma membrane lipid organization. In conclusion, obesity accelerates the skeletal muscle Lands cycle, whose consequence might induce the disruption of plasma membrane organization that suppresses muscle insulin action.

Introduction

Type 2 diabetes is the 7th leading cause of death in the United States (1) and is a major risk factor for cardiovascular disease, the leading cause of death (2). Skeletal muscle is the site of the largest glucose disposal in humans (3, 4). Insulin resistance in skeletal muscle is a necessary precursor to type 2 diabetes (5) and can be triggered by aberrant lipid metabolism (6–8). Several classes of lipids have been implicated in initiating cellular signals that suppress insulin action, but there has not been a clear consensus that these molecules are upregulated in skeletal muscle insulin resistance that occurs in the human population (9–14).

Human skeletal muscle cells (HSkMCs) are primary myoblasts that can be isolated, propagated, and differentiated from muscle biopsies. This in vitro system provides a unique model to study the skeletal muscle lipidome and signaling pathways free of contaminating cell types and circulating factors that affect muscle metabolism. Importantly, these HSkMCs are known to retain their insulin sensitivity phenotype ex vivo, providing a platform to study mechanisms directly relevant to human physiology (15, 16).

In this study, we harvested HSkMCs from subjects who were insulin-sensitive and lean (LN) or insulin-resistant with obesity (OB) (subject characteristics are shown in Supplemental Table 1;

Results

Human primary muscle cells from OB subjects were more insulin resistant in comparison with LN controls (15). A global lipidomic analysis of these LN and OB myotubes revealed many classes of lipids that were differentially abundant (Figure 1B and Supplemental Figure 1, A–L). Among these, several species of lyso-PLs, intermediates of the Lands cycle (17), were lower in OB HSkMCs compared with LN (Figure 1C), a finding not previously described for an insulin-resistant state. While species of many classes of lyso-PLs were reduced with obesity, the ratio of lyso-PL to its parent phospholipid was significantly lower for only lysophosphatidylcholine (lyso-PC)/phosphatidylcholine (PC) (Figure 1D). Previous studies suggest that altering the lyso-PC content of cell membranes is sufficient to alter the physical properties of membranes (18, 19). Consistent with this notion, phospholipid packing of LN myotubes and that of OB myotubes were remarkably different, with OB cells exhibiting more tightly packed membrane head groups compared with LN (Figure 1, E and F). This occurred in the absence of changes in the phospholipid acyl chain saturation index (Supplemental Figure 1M).

What is the molecular mechanism by which obesity promotes a lower abundance of lyso-PL in skeletal muscle? LN and OB HSkMCs used for the lipidomic analyses were cultured ex vivo for several weeks in identical media conditions. Thus, differences in the lipidome of these samples are likely the result of genetic and/or epigenetic influences, instead of hormonal or neuronal inputs that alter cells in vivo. We reasoned that such differential programming might be expected to manifest in gene expression profiles. A whole transcriptome sequencing of LN and OB myotubes revealed that lyso-PC acyltransferase 3 (LPCAT3), an enzyme of the Lands cycle, was more highly expressed with obesity (GEO series accession number GSE162265). These findings were recapitulated in muscle biopsy samples (*not* myotubes) from LN and OB individuals as well as muscle tissue from WT mice fed a high-fat diet (HFD) or db/db mice (Figure 1G). The Lands cycle represents a series of phospholipid-remodeling reactions by which acyl chains become transacylated (17). Of the 13 lyso-PL acyltransferase enzymes (20), LPCAT3 has the highest affinity for 16:0 and 18:0 lyso-PC, consistent with the specificity of reduced lyso-PC/PC ratio (21, 22). Silencing of LPCAT3 in fibroblasts has been shown to increase Akt phosphorylation (23), while incubation of the same cells with 16:0/20:4 PC decreased Akt phosphorylation as a result of plasma membrane–specific effects (24). Mice with a liver-specific deletion of LPCAT3 exhibit enhanced ordering of membranes (25). In both human and mouse skeletal muscle, LPCAT3 is very highly expressed compared with other isoforms of LPCAT (Figure 1H), knockdown increased lyso-PC and decreased PC (Figure 2, B and C), substrates and products of the LPCAT3-mediated reaction, respectively (27, 28). Together, these differences were sufficient to elevate the lyso-PC/PC ratio with LPCAT3 deletion (Figure 2D). Similar effects were seen with lipid species composed of an ethanolamine head group (Supplemental Figure 2, D–F), while the phospholipid saturation index increased with LPCAT3 knockdown (Supplemental Figure 2G). Analogous to differences observed in LN and OB HSkMCs, LPCAT3 deletion reduced phospholipid head group packing (Figure 2, E and F). We then incubated SC and KD cells in a submaximal concentration of insulin to assess insulin signaling events. Strikingly, inhibition of LPCAT3 robustly enhanced insulin signaling with or without insulin (Figure 3A and Supplemental Figure 2H). Notably, the increase occurred at the level of the insulin receptor (IR), a node that is localized in the phospholipid-rich plasma membrane. Consequently, LPCAT3 deletion enhanced insulin-stimulated glycogen synthesis (Figure 3B), suggesting that this intervention increases skeletal muscle insulin sensitivity in vitro (because of low GLUT4:GLUT1 stoichiometry, insulin-stimulated glucose uptake is not an ideal surrogate for insulin sensitivity in C2C12 myotubes). LPCAT3 knockdown also enhanced insulin signaling in HSkMCs from subjects with obesity (Figure 3A).

The organization and clustering of plasma membrane microdomains are linked to the induction of tyrosine kinase signaling events, such as IR signaling (29–31). Because LPCAT3 deletion promoted enhanced insulin signaling at the level of IR phosphorylation, we visualized the organization of plasma membrane microdomains with labeling and patching of plasma membrane GM-1, a known marker of microdomains. Indeed, a greater proportion of C2C12 cells with LPCAT3 knockdown exhibited clustering of GM-1–enriched microdomains (Figure 3C, top, and Figure 3D). Furthermore, LPCAT3 deletion decreased the size of these clusters (Figure 3C, bottom, and Figure 3E), with no differences in total fluorescence from each cell (Supplemental Figure 2I). These data indicate that LPCAT3 inhibition induces a reorganization of plasma membrane microdomains, potentially explaining increased IR phosphorylation.

CI-976 is a pan–lysophospholipid acyltransferase inhibitor (32, 33) that has the ability to disrupt the Lands cycle, similarly to LPCAT3 deletion. To examine the possibility that the insulin-sensitizing effect of LPCAT3 knockdown is attributable to an unknown function of LPCAT3 outside of the Lands cycle, we studied C2C12 myotubes with or without CI-976. Consistent with our findings with LPCAT3 knockdown (Figure 2, E and F), preincubation of WT C2C12 myotubes with CI-976 robustly decreased

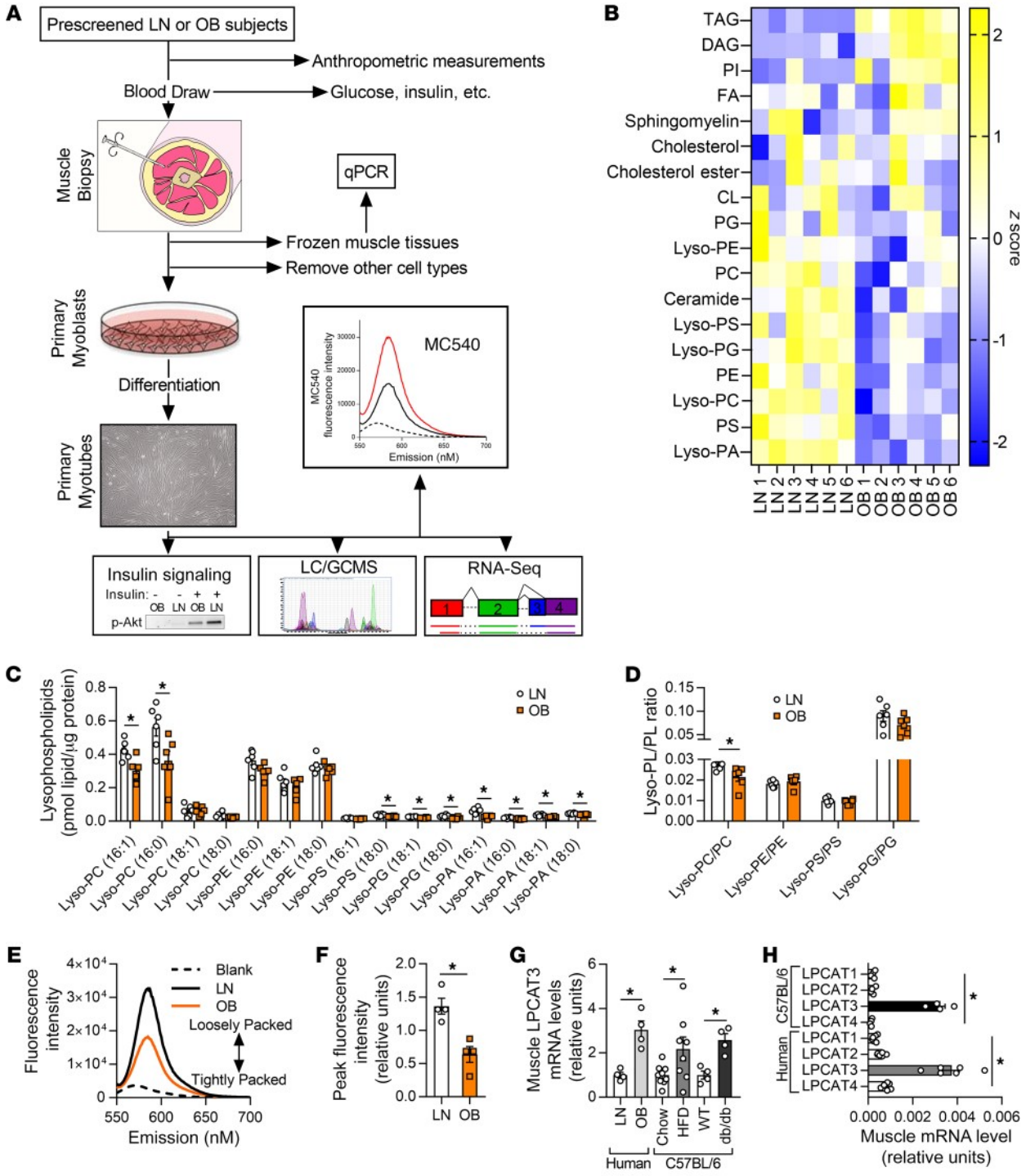

Figure 1. Lipidomic analyses of skeletal muscle samples from human subjects who were lean or with obesity. (**A**) A schematic of the workflow for the

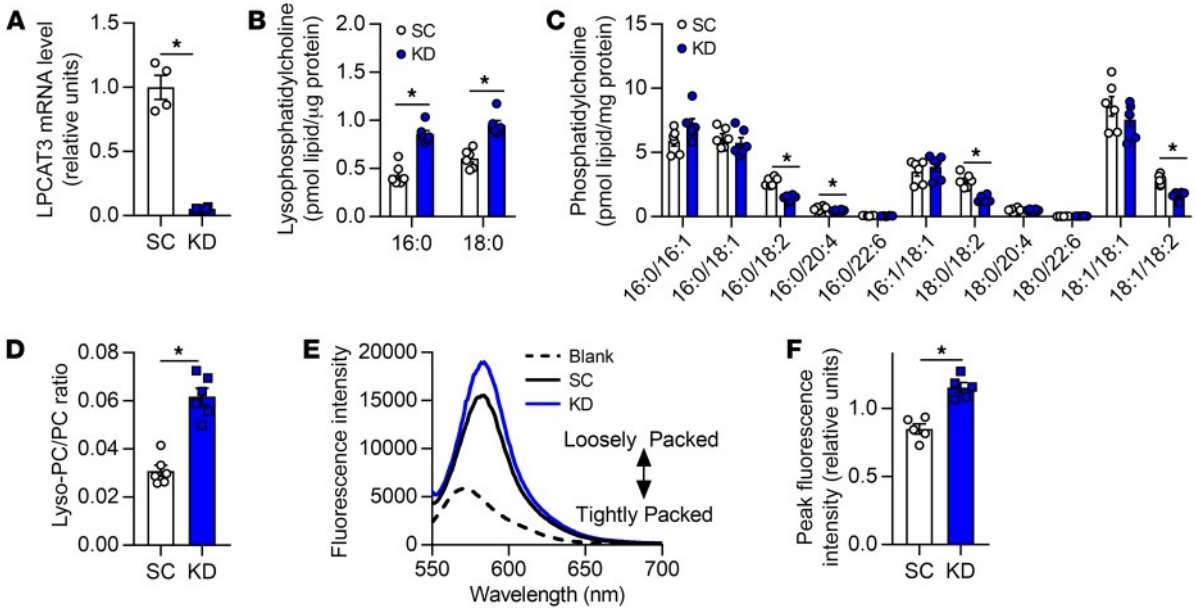

Figure 2. LPCAT3 knockdown alters skeletal muscle membrane phospholipid composition in vitro. (**A**) LPCAT3 mRNA levels in myoblasts infected with lentiviruses expressing shRNA for scrambled (SC) or LPCAT3 sequences (KD) and differentiated into myotubes ($n = 4$). (**B–D**) Lipids were extracted from C2C12 myotubes for analysis between SC and KD cells. Quantification of lyso-PC (**B**), PC (**C**), and total lyso-PC/PC ($n = 6$) (**D**). (**E** and **F**) Quantification of MC540 fluorescence in SC and KD myotubes ($n = 5$). Two-tailed t tests were performed. All data are represented as mean ± SEM. $^*P \leq 0.05$.

inducible skeletal muscle–specific knockout of LPCAT3 (LPCAT3-MKO) were generated by crossing of the HSA-MerCreMer mice (34) with mice with conditional knockout of LPCAT3 (exon 3 of the *Lpcat3* gene flanked with *loxP* sites) (25) (Figure 5A). This strategy successfully yielded mice with suppressed LPCAT3 expression in skeletal muscle without affecting other tissues (Figure 5B), and without compensatory upregulation of other members of the LPCAT family (Figure 5C and Supplemental Figure 3A). Control and LPCAT3-MKO mice gained weight equally when fed HFD (Figure 5D) with no difference in adipose tissue weight at the end of diet intervention (Figure 5E). Food consumption, whole-body oxygen consumption, spontaneous activity, and respiratory exchange ratio were similarly not different between groups (Figure 5, F–I). Fasting glucose and insulin, and glucose tolerance (Figure 5, J and K, and Figure 6A), were unchanged, but circulating insulin during the glucose tolerance test was substantially lower in LPCAT3-MKO mice compared with the control group (Figure 6B).

To evaluate whether improved glycemic efficiency was attributable to greater skeletal muscle insulin sensitivity, we subjected HFD-fed control and LPCAT3-MKO mice to hyperinsulinemic-euglycemic clamping experiments. Similar to results from the glucose assay ex vivo. Indeed, insulin-stimulated skeletal muscle glucose uptake was robustly enhanced in LPCAT3-MKO mice compared with control (Figure 6G). The increase in glucose uptake coincided with augmented insulin-stimulated Akt phosphorylation (Figure 6, H and I), similar to C2C12 and human primary myotubes (Figure 3). These results suggest that inhibition of muscle LPCAT3 increases skeletal muscle insulin sensitivity in vivo.

Similar to results from LPCAT3 knockdown in vitro, muscles from LPCAT3-MKO mice had elevated lyso-PC (16:0 and 18:0) (Figure 7A) and lower levels of PC species known to be the main products of the LPCAT3 reaction (16:0/18:2 and 16:0/22:4) (Figure 7B) (22, 35, 36). As a result, the lyso-PC/PC ratio was approximately 2-fold greater in LPCAT3-MKO mice compared with control (Figure 7C). In contrast, the ratio of lysophosphatidylethanolamine (lyso-PE) to phosphatidylethanolamine (PE) or phospholipid saturation index was unaltered between control and LPCAT3-MKO muscles (Supplemental Figure 3, B–E), similar to the lipidome in LN and OB HSkMCs (Figure 1 and Supplemental Figure 1). Muscles from control and LPCAT3-MKO mice did not differ in mass, length, force-generating capacity, fiber-type distribution, or content of proteins in the electron transport chain (Fig-

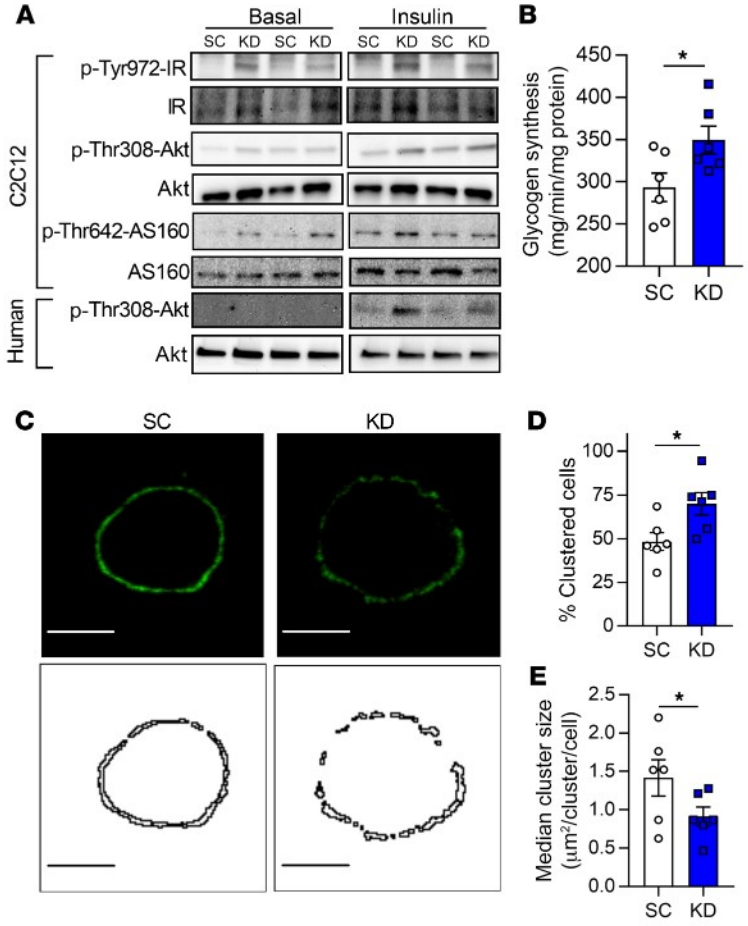

Figure 3. LPCAT3 inhibition enhances skeletal muscle insulin sensitivity in vitro. Myoblasts were infected with lentivirus encoding scrambled (SC) or LPCAT3-knockdown (KD) sequences and differentiated into myotubes. (**A**) Phosphorylation and total protein of IR, Akt, and AS160 were measured via Western blot with insulin (0.6 nM) or without insulin in C2C12 myotubes (top) and human primary skeletal muscle cells (bottom) (image is representative of 3 experiments). (**B**) Glycogen synthesis was quantified in C2C12 cells incubated with insulin (12 nM) (n = 6). (**C**–**E**) GM-1–enriched microdomains were labeled in SC and KD myotubes that had been rounded up. (**C**) Plasma membrane GM-1 localization was visualized (top: fluorescence images; bottom: binary images). Scale bars: 10 μM. (**D**) Cells were scored as clustered or nonclustered between SC and KD myotubes. (**E**) Particle size was measured for each cell in 6 separate experiments, and the median for each experiment was used as a representative of that experiment (n = 35–50 per experiment, 6 separate experiments). Two-tailed t tests were performed. All data are represented as mean ± SEM. *$P \leq 0.05$.

8B). This strategy successfully resulted in LPCAT3 overexpression specific to skeletal muscle (Figure 8C), which was sufficient to accelerate the Lands cycle to reduce lyso-PC (Figure 8D), increase some species of PC (Figure 8E), and reduce the lyso-PC/PC ratio (Figure 8F). LPCAT3-MKI mice had similar body weights to littermate controls when fed standard chow or HFD (Figure 8G). Importantly, LPCAT3-MKI mice were found to be more glucose intolerant compared with controls (Figure 8, H and I). Thus, acceleration of skeletal muscle Lands cycle is sufficient to impair systemic glucose handling.

How does the inhibition of the Lands cycle promote greater insulin action in skeletal muscle? LPCAT3 deficiency enhanced insulin signaling at the level of IR, which was concomitant with altered plasma membrane lipid organization (Figure 3), suggesting that changes in plasma membrane properties may mediate the sion is sufficient to enhance Akt phosphorylation and glucose uptake (46). Indeed, LPCAT3 knockdown substantially increased cav3 content in C2C12 myotubes (Figure 9A). To examine the possibility that the absence of LPCAT3 increases the abundance of lipids in caveolae, we isolated membrane fractions from C2C12 myotubes with or without LPCAT3 deletion and subjected them to further purification by density gradient ultracentrifugation.

Cholesterol and sphingomyelin are 2 classes of lipids that are more highly abundant in the detergent-resistant membrane (DRM; i.e., ordered membrane) fraction compared with the detergent-soluble membrane (DSM) fraction (47). Experiments in WT C2C12 myotubes indicated that fractions 4 and 5 have substantial amounts of total lipid (Supplemental Figure 4A). These fractions were enriched in sphingomyelin and cholesterol, which are known to be conducive to more highly ordered membranes (Supplemen-

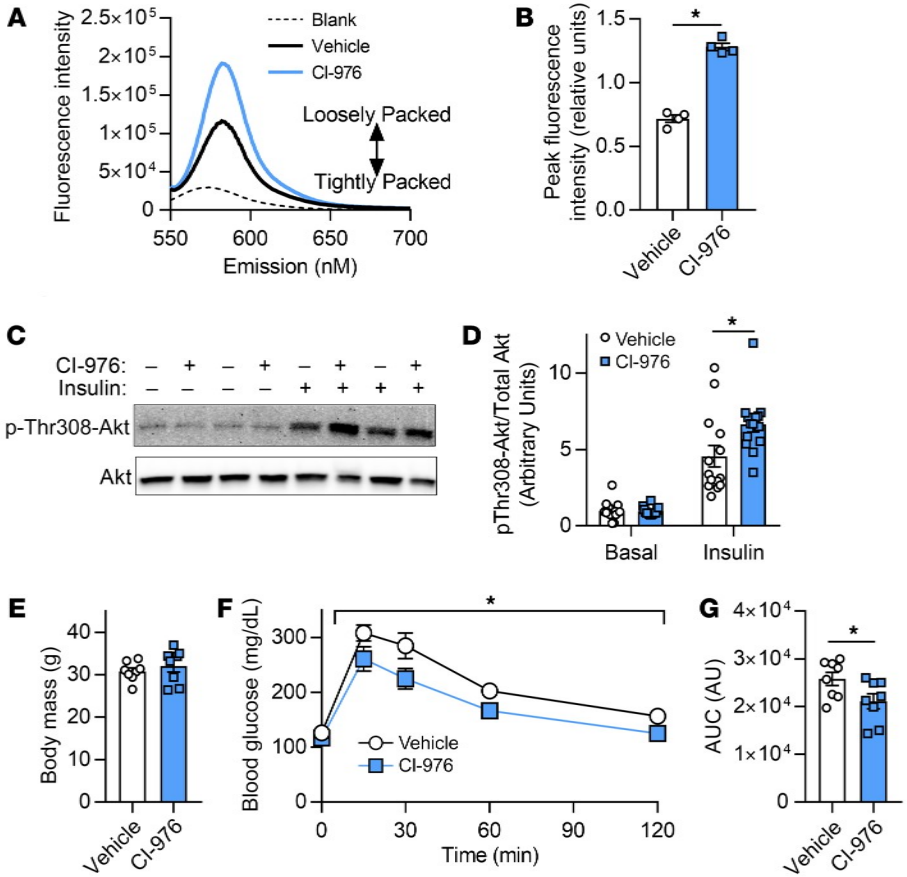

Figure 4. Administration of CI-976 in vitro and in vivo. (**A**–**D**) C2C12 myoblasts were differentiated into myotubes with either CI-976 or vehicle. (**A** and **B**) Quantification of MC540 fluorescence (n = 6). (**C** and **D**) Western blot and quantification of Thr308 phosphorylation and total Akt in the presence (12 nM) and absence of insulin (n = 14; P = 0.024, main effect of insulin). (**E**–**G**) WT C57BL6/J mice were fed with HFD for 6 weeks, with subcutaneous injection for the last 7 days with vehicle (1:9 ethanol/polyethylene glycol) or 30 mg/kg CI-976. Body mass (**E**), intraperitoneal glucose tolerance excursion curves (**F**), and AUC (**G**) from glucose tolerance tests on vehicle-treated or CI-976–injected mice (n = 8 per group). Two-tailed t tests (**B**, **E**, and **G**) or 2-way ANOVA with Šidák's multiple-comparison test (**D** and **F**) was performed. All data are represented as mean ± SEM. *$P \leq 0.05$.

was no enrichment of sphingomyelin or cholesterol in the DRM fraction, which may have been expected given that these lipids induce sequestration of cav3 into caveolae. Consistent with this notion, LPCAT3 deletion was sufficient to elevate lyso-PC in the DRM as well as DSM fractions of the membrane (Figure 9E), with minimal effect on PC species (Supplemental Figure 5A). Similar results were exhibited with lyso-PE and PE (Supplemental Figure 5, B and C). The saturation index of phospholipids was slightly increased in both DRM and DSM fractions, which may also contribute to the increase in the plasma membrane lipid clustering (Supplemental Figure 5D). Thus, LPCAT3 deletion promotes the accumulation of lyso-PC in the DRM fraction, which may contribute to membrane organization.

To test our hypothesis that an increase in membrane organization mediates the insulin-sensitizing effect of LPCAT3 deletion, we incubated C2C12 myotubes with methyl-β-cyclodextrin (MβCD), a cholesterol-depleting compound that disrupts plasma with or without LPCAT3 knockdown. Both EGF and PDGF receptors are localized at the plasma membrane and activate Akt independently of IR (50, 51). Strikingly, LPCAT3 deletion did not augment Akt phosphorylation induced by EGF or PDGF (Figure 10, E and F), suggesting that the effects of LPCAT3 deletion are selective. These findings are consistent with the notion that LPCAT3 deletion enhances insulin signaling by its effect on plasma membrane organization that is relatively specific to IR.

Discussion

Obesity promotes aberrant lipid metabolism in various tissues, including skeletal muscle, where it dampens its ability to respond to circulating insulin and increase glucose uptake. Studies in model organisms have led to the identification of lipotoxic lipids that might promote insulin resistance in various tissues (52, 53), but some studies were unable to validate these mechanisms in human muscles (54, 55). To gain a global understanding of changes that

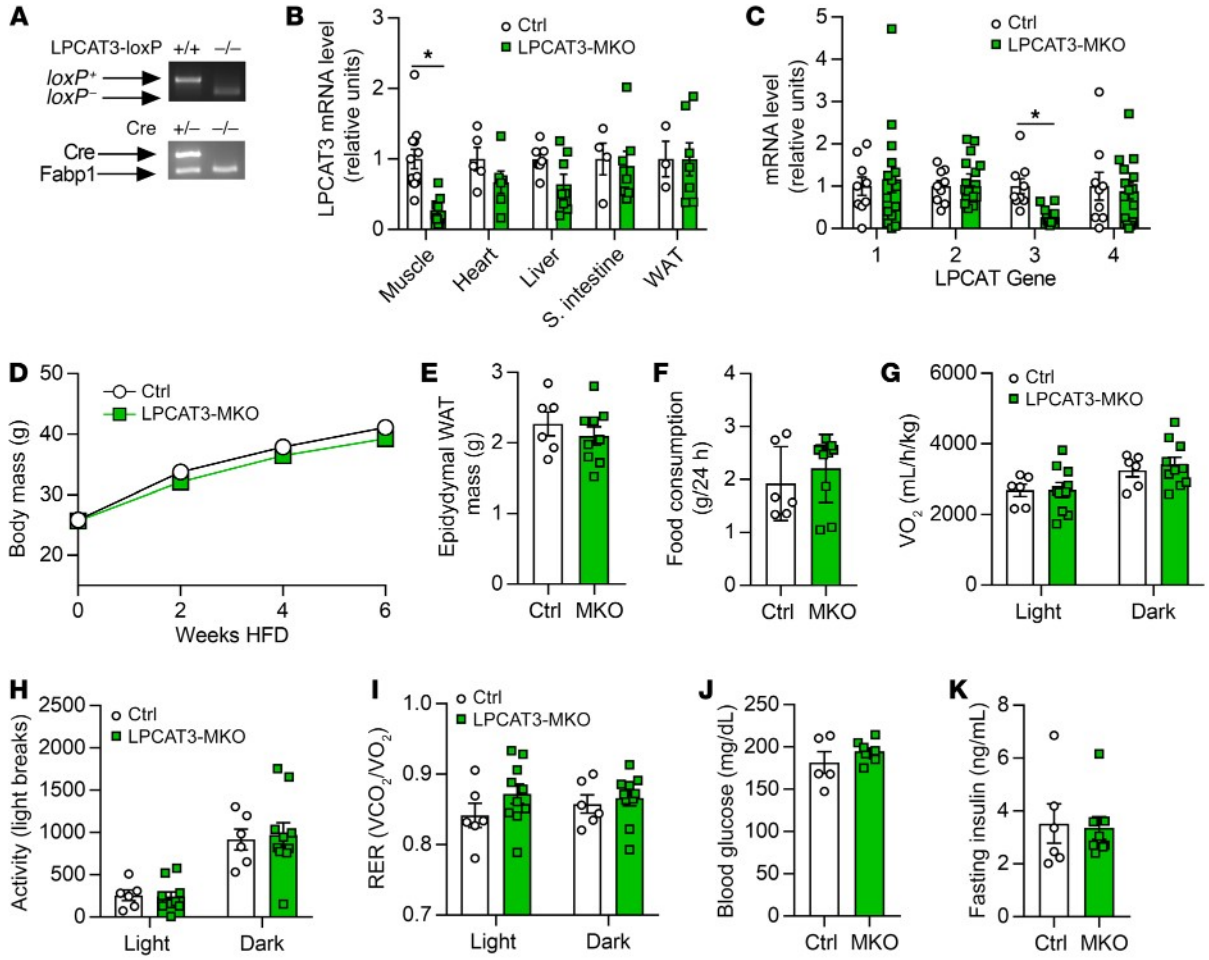

Figure 5. Whole-body phenotyping of LPCAT3-MKO mice. (**A**) Mice with tamoxifen-inducible skeletal muscle–specific Cre recombinase (HSA-MerCreMer$^{+/-}$) were crossed with mice with *loxP* sites flanking exon 3 of the *Lpcat3* gene (LPCAT3cKO$^{+/+}$) to generate skeletal muscle–specific inducible knockout of LPCAT3 (LPCAT3cKO$^{+/+}$; HSA-MerCreMer$^{+/-}$) (LPCAT3-MKO). Littermates (LPCAT3cKO$^{+/+}$; HSA-MerCreMer$^{-/-}$) (Ctrl) were used as control mice for all experiments. (**B**) LPCAT3 mRNA in tibialis anterior (Muscle), heart, liver, small intestine, and inguinal white adipose tissue (WAT) (muscle: Ctrl n = 12, MKO n = 15; heart: Ctrl n = 5, MKO n = 6; liver: Ctrl n = 7, MKO n = 8; small intestine: Ctrl n = 4, MKO n = 7; WAT: Ctrl n = 3, MKO n = 7). (**C**) mRNA of all LPCAT isoforms in tibialis anterior muscles of Ctrl and LPCAT3-MKO mice (Ctrl n = 9, MKO n = 14). (**D**) Body mass during HFD feeding in Ctrl and LPCAT3-MKO mice (Ctrl n = 8, MKO n = 11). (**E**) Epididymal WAT mass (Ctrl n = 6, MKO n = 9). (**F**–**I**) Ctrl and LPCAT3-MKO mice were placed in metabolic chambers for measurement of food consumption (**F**), VO_2 (**G**), activity (**H**), and respiratory exchange ratio (RER) (**I**) (Ctrl n = 6, MKO n = 10). (**J**) Fasting glucose (Ctrl n = 5, MKO n = 9). (**K**) Fasting insulin (Ctrl n = 6, MKO n = 9). All data except those in **A** are from HFD-fed mice. Two-tailed t tests (**B**, **C**, **E**, **F**, **J**, and **K**) or 2-way ANOVA with Šidák's multiple-comparison test (**D** and **G**–**I**) was performed. All data are represented as mean ± SEM. $^*P \leq 0.05$.

utable to diet-induced activation of LXRs and PPARs (22, 56, 57). Indeed, we found that skeletal muscle–specific overexpression of LPCAT3 was sufficient to augment glucose intolerance induced by HFD feeding. In contrast, inhibition of LPCAT3 enhances insulin signaling at the level of IR to improve skeletal muscle insulin alter EGF or PDGF sensitivity, suggesting some specificity for IR. LPCAT3 deletion did not appear to have an overly adverse effect on skeletal muscle, including mass, fiber type, or force-generating capacity. It would be of substantial interest to pursue implications of altered Lands cycle and/or plasma membrane organization in

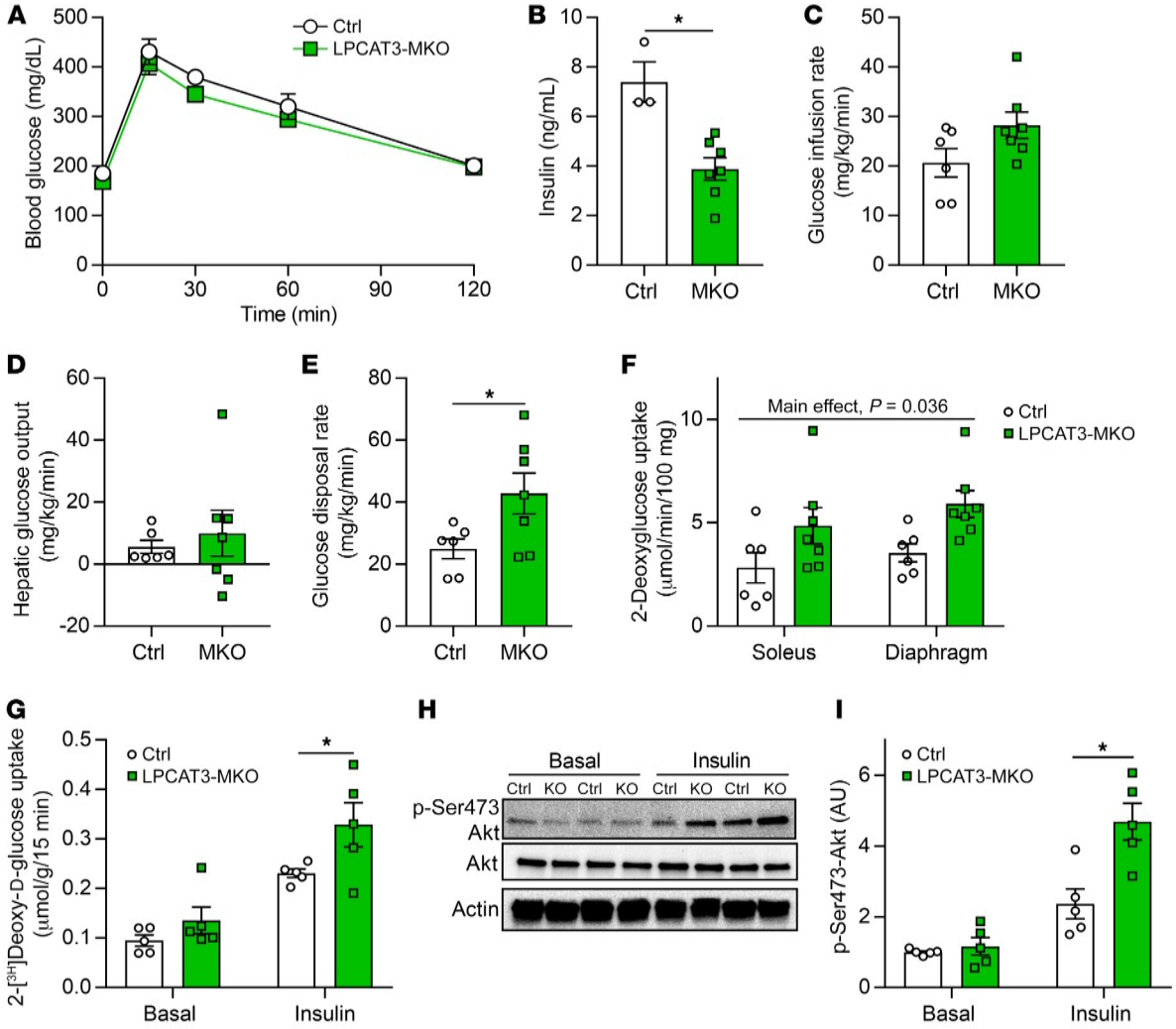

Figure 6. LPCAT3-MKO mice are protected from diet-induced skeletal muscle insulin resistance. (**A**) Intraperitoneal glucose tolerance test (Ctrl $n = 6$, MKO $n = 8$). (**B**) Serum insulin at the 30-minute time point of the glucose tolerance test (Ctrl $n = 3$, MKO $n = 8$). (**C**–**F**) Hyperinsulinemic-euglycemic clamps were performed in conscious unrestrained mice (Ctrl $n = 6$, MKO $n = 7$). (**C**) Glucose infusion rate required to maintain constant blood glucose of 150 mg/dL during clamp phase. (**D**) Hepatic glucose output during the clamp phase. (**E**) Rate of whole-body glucose disposal during the clamp phase. (**F**) ^{14}C-2-deoxyglucose uptake quantification in soleus and diaphragm muscles during the clamped state. (**G**–**I**) Soleus muscles were dissected and incubated with or without 200 μU/mL of insulin. (**G**) Ex vivo 2-deoxyglucose uptake ($n = 5$). (**H** and **I**) Ser473 phosphorylation and total Akt ($n = 5$). All data are from HFD-fed mice. Two-way ANOVA with Šidák's multiple-comparison test (**A**, **F**, **G**, and **I**) or 2-tailed t tests (**B**–**E**) were performed. All data are represented as mean ± SEM. *$P \leq 0.05$.

studies performed in human samples, suggesting that this mechanism may be directly involved in the pathogenesis of skeletal muscle insulin resistance in human obesity. We are also interested in examining whether obesity induces similar changes in plasma

biopsy from the vastus lateralis were collected. A portion of the biopsy sample was frozen immediately, and another portion was used to isolate primary muscle cells.

Cell culture. Primary human skeletal muscle cells (HSkMCs) were

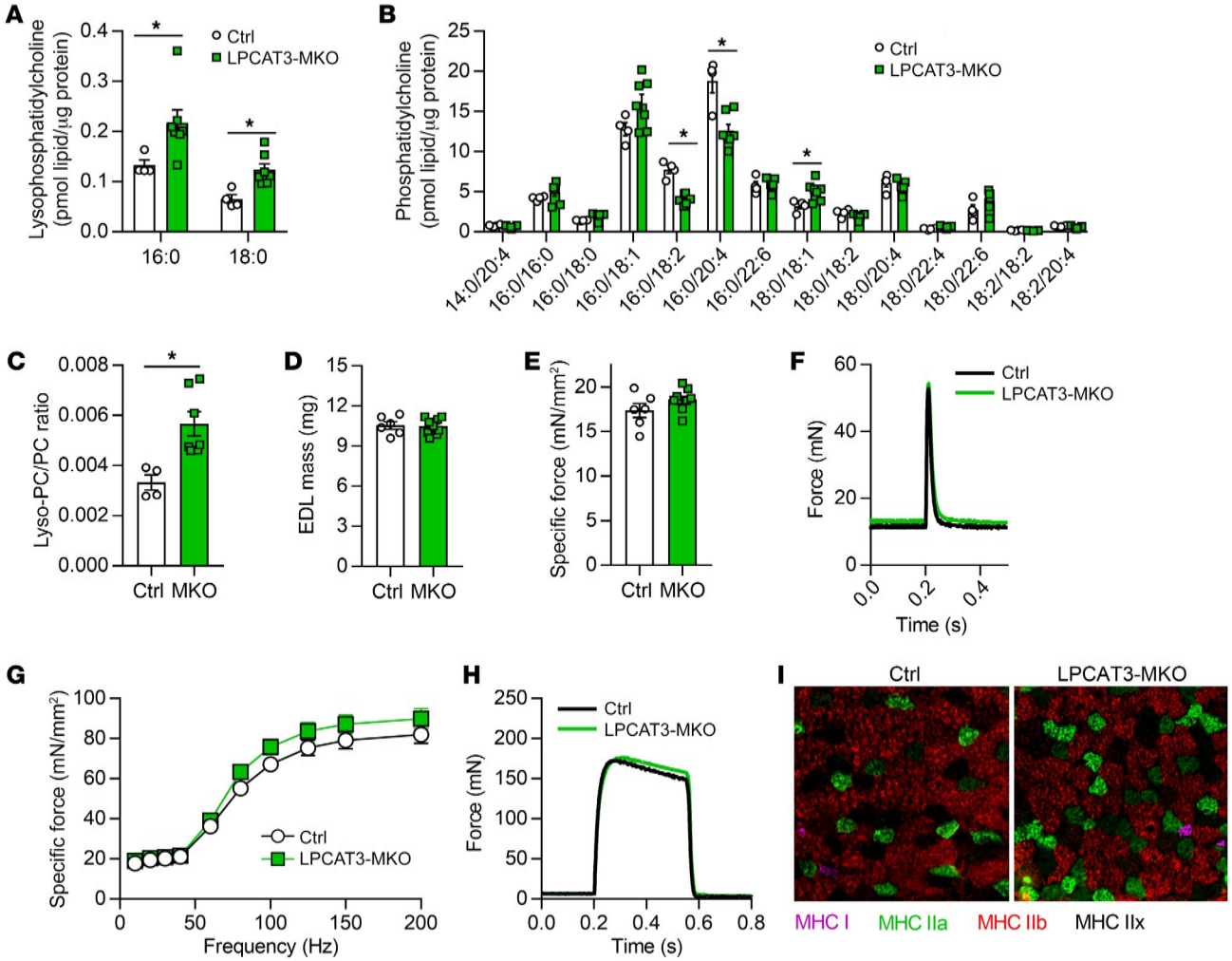

Figure 7. Skeletal muscle lipid composition and contractility in LPCAT3-MKO mice. (**A**–**C**) Lipids were extracted from gastrocnemius muscles of Ctrl and LPCAT3-MKO mice for mass spectrometric analysis. Quantification of lyso-PC (**A**), PC (**B**), and total lyso-PC/PC (**C**) (Ctrl $n = 4$, MKO $n = 7$). (**D**–**I**) Extensor digitorum longus (EDL) muscles of Ctrl and LPCAT3-MKO mice were dissected for measurement of mass (**D**), force produced with a pulse stimulation (**E** and **F**), force produced with tetanic stimulation ranging from 10 to 200 Hz (**G** and **H**) (**H**, force tracing at 200 Hz stimulation) (Ctrl $n = 6$, MKO $n = 9$), and skeletal muscle fiber type (MHC I, pink; MHC IIa, green; MHC IIb, red; MHC IIx, negative) (**I**). Two-tailed t tests (**A**–**E**) or 2-way ANOVA with Šidák's multiple-comparison test (**G**) was performed. All data are represented as mean ± SEM. $^*P \leq 0.05$.

with L-glutamine and 110 mg/L sodium pyruvate; Gibco 11885-084) supplemented with 2% horse serum (defined; VWR 16777), and 0.1% penicillin-streptomycin. For experiments with CI-976, C2C12 myoblasts were differentiated with either 10 μM of CI-976 or equal-volume DMSO (vehicle). For experiments with MβCD, cells were incubated with 10 mM (1320 g/mol) MβCD for 1 hour directly dissolved into medium. For experiments with PDGF or EGF, C2C12 myotubes were incubated

Mass spectrometry. Global lipidomic analyses of LN and OB HSkMCs were performed at the Mass Spectrometry Resource at the Washington University School of Medicine (15). Extracted lipids with internal standards were analyzed with a Thermo Vantage triple-quadrupole mass spectrometer or a Thermo Trace GC Ultra mass spectrometer. Targeted lipidomic analyses for C2C12 myotubes and mouse skeletal muscles were conducted in the Metabolomics Core at the University of

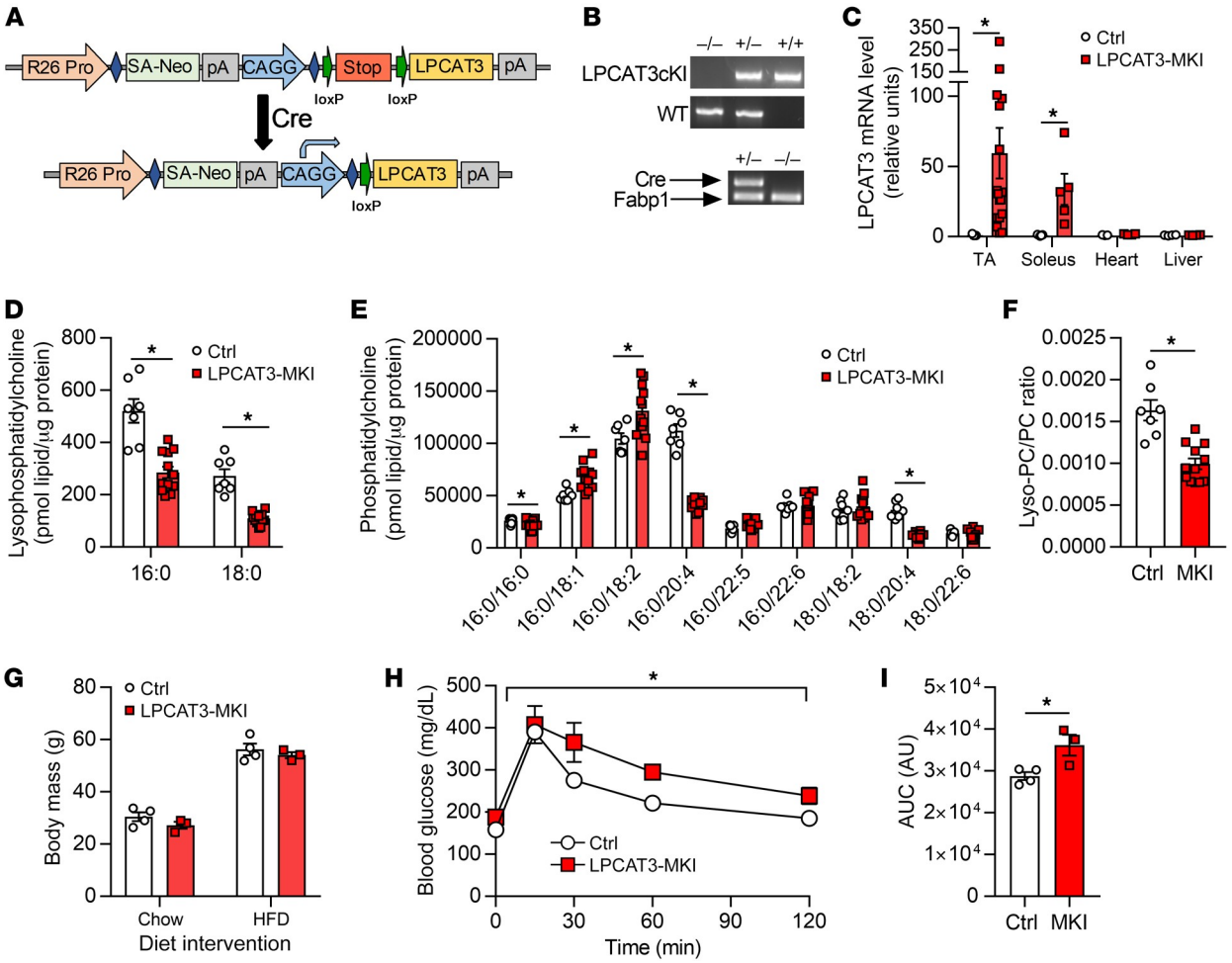

Figure 8. Generation and characterization of mice with skeletal muscle–specific overexpression of LPCAT3 (LPCAT3-MKI). (**A**) Schematic of mouse conditional LPCAT3 knockin (LPCAT3cKI$^{+/+}$) with insertion of mouse LPCAT3 cDNA sequence in the Rosa26 locus preceded by a stop codon flanked with *loxP* sites. (**B**) Genotyping of LPCAT3cKI$^{+/+}$ mice crossed with HSA-MCM$^{+/-}$ mice to generate LPCAT3cKI$^{+/-}$; HSA-MCM$^{-/-}$ (Ctrl) or LPCAT3cKI$^{+/-}$; HSA-MCM$^{+/-}$ (LPCAT3-MKI) mice. (**C**) Quantitative RT-PCR of LPCAT3 in tibialis anterior (TA) (Ctrl n = 9, MKI n = 17), soleus (Ctrl n = 5, MKI n = 5), heart (Ctrl n = 3, MKI n = 4), and liver (Ctrl n = 4, MKI n = 4). (**D**–**I**) Lipids were extracted from TA muscles and quantified for lyso-PC (**D**), PC (**E**), and lyso-PC/PC ratio (**F**) (Ctrl n = 7, MKI n = 12). (**G**) Body mass of Ctrl and LPCAT3-MKI mice fed a standard chow diet or after 12 weeks of HFD feeding. (**H** and **I**) Intraperitoneal glucose tolerance test (**H**) and AUC (**I**) from glucose tolerance test between Ctrl and LPCAT3-MKI mice after HFD feeding (Ctrl n = 4, MKI n = 3). Two-tailed t tests (**C**–**G** and **I**) or 2-way ANOVA (**H**) was performed. All data are represented as mean ± SEM. *$P \leq 0.05$.

14025092) before resuspension in a cuvette with HBSS. MC540 in DMSO was added at a final concentration of 0.2 μM, and after a 10-minute dark incubation, an emission scan was performed ranging from 550 to 750 nm with fluorescence excitation set at 540 nm on a PTI QuantaMaster 6000 Fluorimeter.

Lentivirus-mediated knockdown of LPCAT3. LPCAT3 expression HSkMCs or C2C12 cells for 48 hours. To ensure that only cells infected with shRNA vectors were viable, cells were selected with puromycin throughout differentiation.

Western blot. Whole muscle or cells were homogenized and Western blots were performed as previously described (59). Protein homogenates were analyzed for abundance of phosphorylated Tyr972–insu-

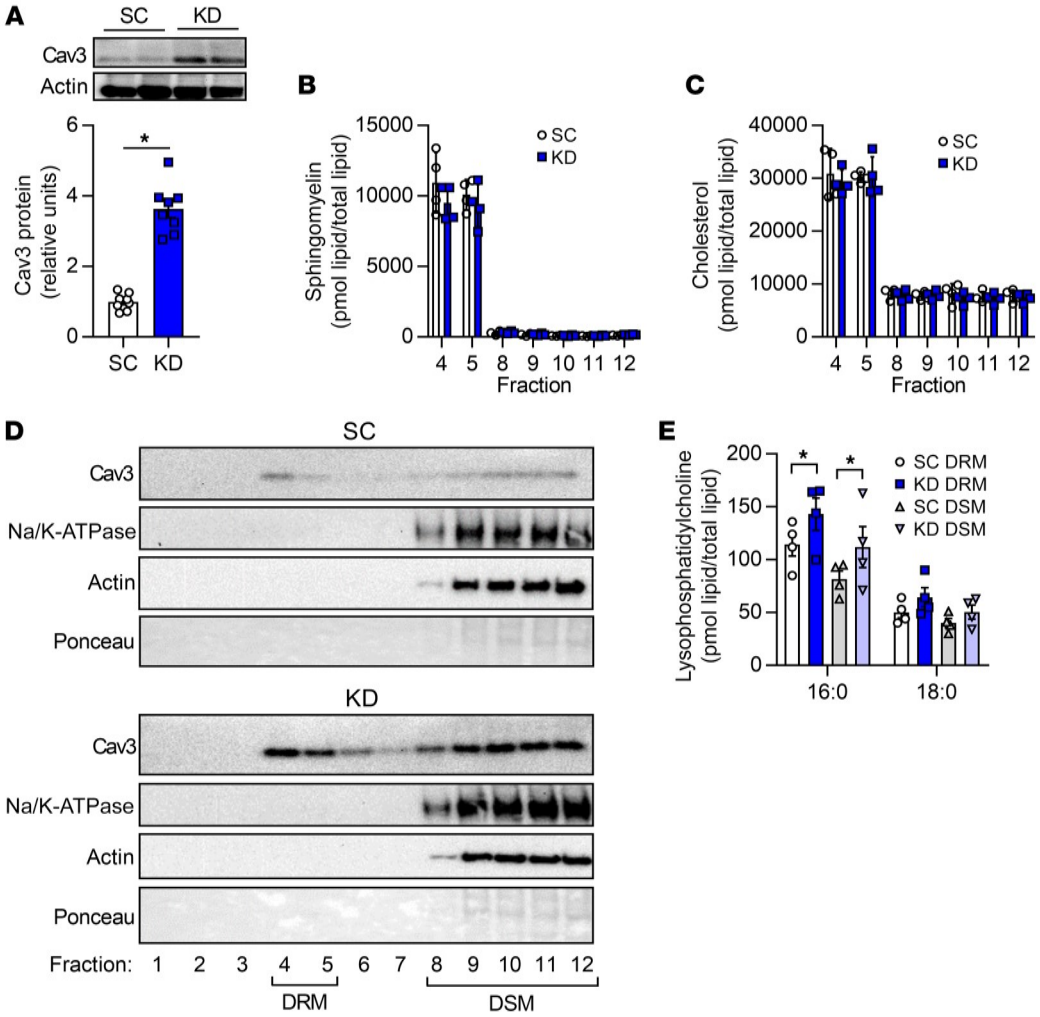

Figure 9. LPCAT3 deletion alters plasma membrane organization. C2C12 cells were infected with lentiviruses expressing shRNA for scrambled (SC) or LPCAT3 (KD) sequences and differentiated into myotubes. (**A**) Caveolin-3 (cav3) protein content. (**B** and **C**) Detergent-resistant membranes (DRMs; fractions 4 and 5) and detergent-soluble membranes (DSMs; fractions 8–12) were isolated, and lipids were extracted for quantification of sphingomyelin (**B**) and cholesterol (**C**) ($n = 4$). (**D**) Cav3, Na/K-ATPase, actin, and total protein content were assessed via Western blot in all fractions from the sucrose gradient (image is representative of 4 experiments). (**E**) Lyso-PC levels in DSM and DRM isolations ($n = 4$). Two-tailed t tests (**A**–**C**) or 2-way ANOVA with Šidák's multiple-comparison test (**E**) was performed. All data are represented as mean ± SEM. $^*P \leq 0.05$.

Glycogen synthesis. The glycogen synthesis rate was quantified as previously described (64, 65). Briefly, cells were incubated in medium containing D-[U-^{14}C]glucose with insulin (12 nM) or without insulin for 2 hours at 37°C. Cells were then washed with ice-cold PBS and homogenized for 1 hour with 0.05% SDS. Part of the lysate was used for a protein assay, and the other was combined with 2 mg carrier glycogen and incubated at 100°C for 1 hour. Ice-cold ethanol (100%) was added

etal muscle–specific LPCAT3 knockout; LPCAT3-MKO) mice. Conditional-LPCAT3-knockin (LPCAT3cKI$^{+/+}$) mice were generated by insertion of a mouse LPCAT3 cDNA that was preceded by a lox-STOP-lox sequence into the Rosa26 locus of the genome. LPCAT3cKI$^{+/+}$ mice were then crossed with HSA-MerCreMer$^{+/-}$ mice to generate LPCAT3cKI$^{+/-}$; HSA-MerCreMer$^{-/-}$ (control) and LPCAT3cKI$^{+/-}$; HSA-MerCreMer$^{+/-}$ (skeletal muscle–specific LPCAT3 knockin; LPCAT3-

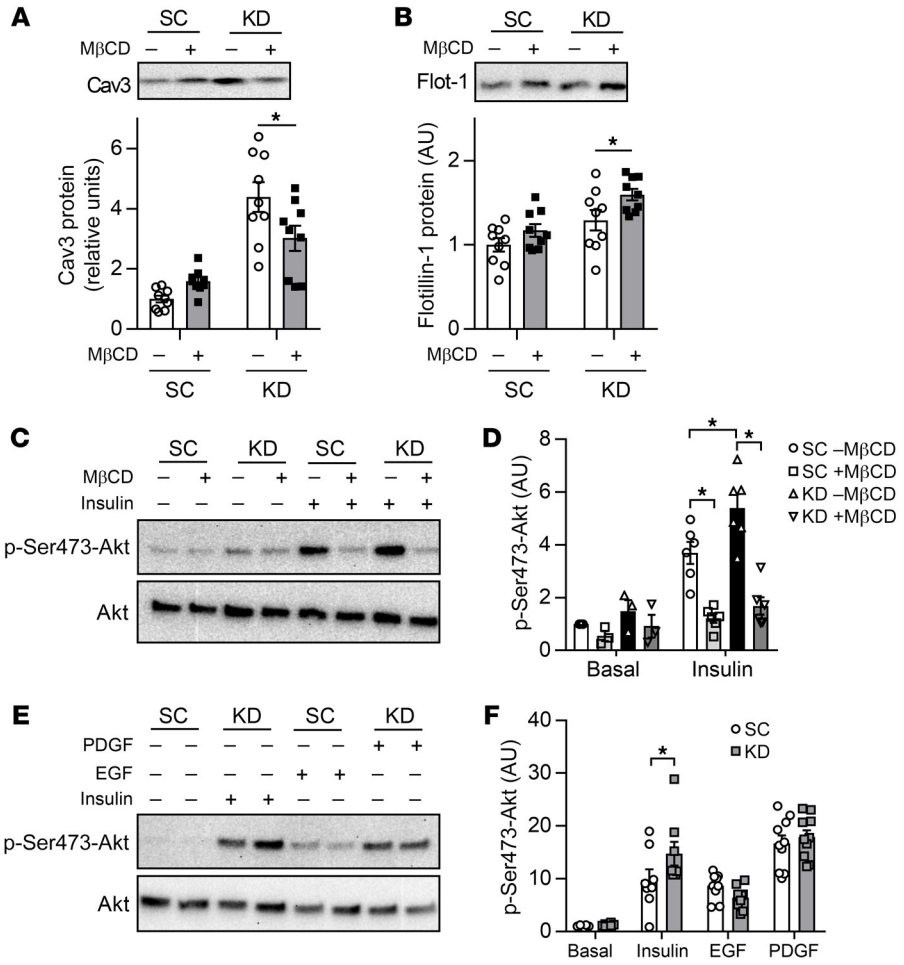

Figure 10. Disruption of caveolae is sufficient to normalize insulin signaling with LPCAT3 knockdown. C2C12 myoblasts were infected with lentivirus expressing shRNA for scrambled (SC) or LPCAT3-knockdown (KD) sequences and were differentiated into myotubes. (**A**–**D**) Myotubes were incubated with or without 10 mM of methyl-β-cyclodextrin (MβCD) for 1 hour. (**A** and **B**) MβCD successfully depletes cav3 ($P < 0.001$, main effect of LPCAT3 knockdown) but not flotillin-1 ($P = 0.003$, main effect of LPCAT3 knockdown; $P = 0.01$, main effect of MβCD) ($n = 9$). (**C** and **D**) Cells were incubated in the presence (0.6 nM) or absence of insulin and were blotted for total or Ser473 phosphorylation of Akt ($n = 3$ basal, $n = 6$ insulin). (**E** and **F**) C2C12 myotubes were incubated in the absence or presence of either PDGF (2.5 ng/mL), EGF (100 ng/mL), or insulin (12 nM) and were blotted for total or Ser473 phosphorylation of Akt (basal and insulin, $n = 8$; PDGF and EGF, $n = 10$). Two-way ANOVA with Šidák's multiple-comparison test was performed. All data are represented as mean ± SEM. $^*P \leq 0.05$.

tour 7151H). In a separate set of experiments, mice were injected with 1 mg glucose per gram body mass, and blood was taken from the facial vein at the 30-minute time point for insulin quantification.

Serum insulin and glucose quantification. Blood was collected from the facial vein either before anesthesia or at the 30-minute time point of the glucose tolerance test. Blood was then placed at room temperature for 20 minutes to allow for clotting before centrifugation at 2000*g* for 10 minutes at 4°C. The supernatant (serum) was placed in a separate tube and stored at –80°C until analysis.

Serum glucose was quantified using a colorimetric assay. A glucose standard curve was generated (MilliporeSigma, G6918), and serum samples were mixed with a PGO enzyme (MilliporeSigma, P7119) and colorimetric substrate (MilliporeSigma, F5803) and measured at OD_{450} on a plate reader. Serum insulin was quantified with an insulin mouse

Ex vivo skeletal muscle [³H]2-deoxy-D-glucose uptake. Ex vivo glucose uptake was measured in the soleus muscle as previously described (69, 70). In brief, soleus muscles were dissected and placed in a recovery buffer (KHB with 0.1% BSA, 8 mM glucose, and 2 mM mannitol) at 37°C for 10 minutes. After incubation in recovery buffer, muscles were moved to preincubation buffer (KHB with 0.1% BSA, 2 mM sodium pyruvate, and 6 mM mannitol) with or without 200 μU/mL insulin for 15 minutes. After preincubation, muscles were placed in incubation buffer (KHB with 0.1% BSA, 9 mM [¹⁴C]mannitol, 1 mM [³H]2-deoxyglucose) with or without 200 μU/mL insulin for 15 minutes. Contralateral muscles were used for basal or insulin-stimulated measurements. After incubation, muscles were blotted dry on ice-cold filter paper, snap-frozen, and stored at –80°C until analyzed with liquid scintillation counting.

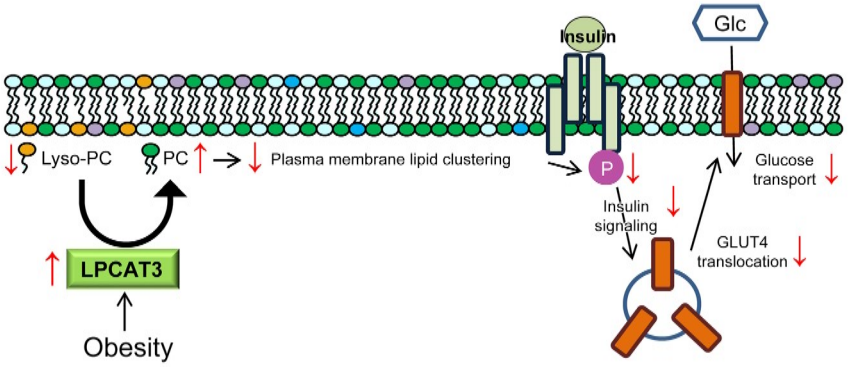

Figure 11. A proposed mechanism of action by which LPCAT3 promotes diet-induced skeletal muscle insulin resistance. Obesity leads to acceleration of the Lands cycle through upregulation of LPCAT3. Increased LPCAT3 activity decreases lyso-PC and increases PC content, which leads to decreased microdomain clustering on the plasma membrane. Disorganization of plasma membrane lipid organization leads to attenuated insulin receptor signaling and decreased insulin-stimulated glucose uptake.

with M.O.M. mouse IgG Blocking Reagent (Vector Laboratories, MKB-2213), myofiber sections were incubated for 1 hour with concentrated BA.D5, SC.71, and BF.F3 (all 1:100; DSHB) and laminin (1:200; MilliporeSigma, L9393) in 2.5% normal horse serum. To visualize laminin (for fiber border), myosin heavy chain I (MHC I), MHC IIa, and MHC IIb, slides were incubated for 1 hour with the following secondary antibodies, respectively: AMCA (1:250; Vector Laboratories, CI-1000), Alexa Fluor 647 (1:250; Invitrogen, A21242), Alexa Fluor 488 (1:500; Invitrogen, A21121), and Alexa Fluor 555 (1:500; Invitrogen, A21426). Negatively stained fibers were considered MHC IIx. After staining, slides were coverslipped with mounting medium (Vector Laboratories, H-1000). Stained slides were imaged with a fully automated wide-field light microscope (Nikon Corp.) with a 10× objective lens. Images were captured using a high-sensitivity Andor Clara CCD camera.

Administration of CI-976 in vivo. CI-976 was administered as previously described (75). Briefly, C57BL/6J mice were fed a high-fat diet (Envigo, TD.88137) for 6 weeks before 7 consecutive days of subcutaneous injection of either vehicle (1:9 vol/vol of ethanol/polyethylene glycol; Rigaku Reagents, 1008414) or CI-976 at a final concentration of 30 mg/kg.

GM-1 labeling and imaging. GM-1 clusters were labeled using a Vybrant Alexa Fluor 488 Lipid Raft Labeling Kit (Thermo Fisher Scientific, V34404) as previously described (76). Briefly, 2 million myotubes were incubated in 1 mL in ice-cold starvation medium with 0.8 μg/mL fluorescent cholera toxin subunit B conjugate (CT-B) for 10 minutes. CT-B conjugates were then cross-linked with an anti–CT-B antibody (1:200) in ice-cold starvation medium for 15 minutes. Cells were fixed cells per group were analyzed and the median was taken as a representative of that experiment.

Detergent-resistant membrane isolation. Detergent-resistant membranes (DRMs) and detergent-soluble membranes (DSMs) were isolated as previously described (79). Briefly, 2 × 15 cm plates of cells were scraped in ice-cold PBS and then pelleted. Cells were resuspended in 1 mL of cold homogenization buffer (Mes-buffered saline [MBS], 1% Triton X wt/vol, and protease and phosphatase inhibitor) and passed through a 23-gauge needle 6 times before incubation at 4°C for 30 minutes. MBS was added to the homogenate until a volume of 2.5 mL was reached, then mixed with 2.5 mL of 90% sucrose in MBS, and 4 mL of this mixture was added to an ultracentrifuge tube (Beckman Coulter, 344061). A sucrose gradient was generated by addition of 4 mL of 35% sucrose followed by 4 mL of 5% sucrose. Samples were then centrifuged at 100,000*g* at 4°C for 20 hours in a swinging bucket rotor (Beckman L8-M Ultracentrifuge, SW28 Rotor).

Statistics. Statistical analysis was performed using Prism 7 software (GraphPad). Two-tailed Student's *t* tests were performed with data composed of 2 groups, and 2-way ANOVA followed by Šidák's multiple-comparison test was performed for more than 2 groups. All data are mean ± SEM, and statistical significance was set at P less than 0.05.

Study approval. The experimental protocol was approved by the Internal Review Board for Human Research at East Carolina University. Informed consent was obtained prior to inclusion in the study.

Animal experiments were approved by the University of Utah Institutional Animal Care and Use Committee.

Author contributions

PJF and KF contributed to study concept design and wrote the manuscript. JAH performed human muscle biopsies. JMJ and MJD contributed to study design and data analysis. XR, PT, TDG, JMM, and PJF developed and maintained the mouse models. PJF and WLH performed hyperinsulinemic-euglycemic clamp procedure and analysis. JAM, JEC, HS, and JT performed mass spectrometry analyses. PJF, KF, and SRS performed analyses of the physical properties of phospholipid membranes. ARPV and PJF performed analysis of muscle force production. PS performed muscle histology measurements. PJF performed all biochemical assays and metabolic phenotyping measurements. KCK and AJL performed correlation analyses with 106 mouse strains. JAH, PT, JT, JEC, MJD, SRS, and WLH edited the manuscript.

S10-OD021505, and U54-DK110858. The Washington University Biomedical MS Resource is supported by US Public Health Services grants P41-GM103422, P30-DK020579, and P30-DK056341.

Address correspondence to: Katsuhiko Funai, Diabetes and Metabolism Research Center, 15 N, 2030 E, Salt Lake City, Utah 84112, USA. Phone: 801.585.1781; Email: kfunai@utah.edu.

1. Heron M. Deaths: leading causes for 2017. *Natl Vital Stat Rep*. 2019;68(6):1–77.
2. Huo X, et al. Risk of non-fatal cardiovascular diseases in early-onset versus late-onset type 2 diabetes in China: a cross-sectional study. *Lancet Diabetes Endocrinol*. 2016;4(2):115–124.
3. DeFronzo RA, et al. The effect of insulin on the disposal of intravenous glucose. Results from indirect calorimetry and hepatic and femoral venous catheterization. *Diabetes*. 1981;30(12):1000–1007.
4. Thiebaud D, et al. The effect of graded doses of insulin on total glucose uptake, glucose oxidation, and glucose storage in man. *Diabetes*. 1982;31(11):957–963.
5. DeFronzo RA, Tripathy D. Skeletal muscle insulin resistance is the primary defect in type 2 diabetes. *Diabetes Care*. 2009;32(suppl 2):S157–S163.
6. Dube JJ, et al. Effects of acute lipid overload on skeletal muscle insulin resistance, metabolic flexibility, and mitochondrial performance. *Am J Physiol Endocrinol Metab*. 2014;307(12):E1117–E1124.
7. Manco M, et al. Insulin resistance directly correlates with increased saturated fatty acids in skeletal muscle triglycerides. *Metabolism*. 2000;49(2):220–224.
8. Lee JS, et al. Saturated, but not n-6 polyunsaturated, fatty acids induce insulin resistance: role of intramuscular accumulation of lipid metabolites. *J Appl Physiol (1985)*. 2006;100(5):1467–1474.
9. Chavez JA, Summers SA. Characterizing the effects of saturated fatty acids on insulin signaling and ceramide and diacylglycerol accumulation in 3T3-L1 adipocytes and C2C12 myotubes. *Arch Biochem Biophys*. 2003;419(2):101–109.
10. Bergman BC, et al. Localisation and composition of skeletal muscle diacylglycerol predicts insulin resistance in humans. *Diabetologia*. 2012;55(4):1140–1150.
11. Perreault L, et al. Intracellular localization of diacylglycerols and sphingolipids influences insulin sensitivity and mitochondrial function in human skeletal muscle. *JCI Insight*. 2018;3(3):96805.
12. Adams JM 2nd, et al. Ceramide content is increased in skeletal muscle from obese insulin-resistant humans. *Diabetes*. 2004;53(1):25–31.
13. Schmitz-Peiffer C, et al. Ceramide generation is sufficient to account for the inhibition of the insulin-stimulated PKB pathway in C2C12 skeletal muscle cells pretreated with palmitate. *J Biol*
humans. *Cell Metab*. 2005;2(4):251–261.
17. Lands WE. Metabolism of glycerolipides; a comparison of lecithin and triglyceride synthesis. *J Biol Chem*. 1958;231(2):883–888.
18. Fink KL, Gross RW. Modulation of canine myocardial sarcolemmal membrane fluidity by amphiphilic compounds. *Circ Res*. 1984;55(5):585–594.
19. Bing RJ, et al. Membrane function and vascular reactivity. *Biosci Rep*. 1993;13(2):61–67.
20. Hishikawa D, et al. Diversity and function of membrane glycerophospholipids generated by the remodeling pathway in mammalian cells. *J Lipid Res*. 2014;55(5):799–807.
21. Kazachkov M, et al. Substrate preferences of a lysophosphatidylcholine acyltransferase highlight its role in phospholipid remodeling. *Lipids*. 2008;43(10):895–902.
22. Zhao Y, et al. Identification and characterization of a major liver lysophosphatidylcholine acyltransferase. *J Biol Chem*. 2008;283(13):8258–8265.
23. Pein H, et al. Vitamin A regulates Akt signaling through the phospholipid fatty acid composition. *FASEB J*. 2017;31(10):4566–4577.
24. Koeberle A, et al. Arachidonoyl-phosphatidylcholine oscillates during the cell cycle and counteracts proliferation by suppressing Akt membrane binding. *Proc Natl Acad Sci U S A*. 2013;110(7):2546–2551.
25. Rong X, et al. Lpcat3-dependent production of arachidonoyl phospholipids is a key determinant of triglyceride secretion. *Elife*. 2015;4:e06557.
26. Parks BW, et al. Genetic architecture of insulin resistance in the mouse. *Cell Metab*. 2015;21(2):334–347.
27. Eto M, et al. Lysophosphatidylcholine acyltransferase 3 is the key enzyme for incorporating arachidonic acid into glycerophospholipids during adipocyte differentiation. *Int J Mol Sci*. 2012;13(12):16267–16280.
28. Martin SA, et al. Measurement of lysophospholipid acyltransferase activities using substrate competition. *J Lipid Res*. 2014;55(4):782–791.
29. Li S, et al. Expression and characterization of recombinant caveolin. Purification by polyhistidine tagging and cholesterol-dependent incorporation into defined lipid membranes. *J Biol Chem*. 1996;271(1):568–573.
30. Murata M, et al. VIP21/caveolin is a cholesterol-binding protein. *Proc Natl Acad Sci U S A*. 1995;92(22):10339–10343.
2005;118(Pt 14):3061–3071.
34. McCarthy JJ, et al. Inducible Cre transgenic mouse strain for skeletal muscle-specific gene targeting. *Skelet Muscle*. 2012;2(1):8.
35. Hishikawa D, et al. Discovery of a lysophospholipid acyltransferase family essential for membrane asymmetry and diversity. *Proc Natl Acad Sci U S A*. 2008;105(8):2830–2835.
36. Gijon MA, et al. Lysophospholipid acyltransferases and arachidonate recycling in human neutrophils. *J Biol Chem*. 2008;283(44):30235–30245.
37. Vainio S, et al. Dynamic association of human insulin receptor with lipid rafts in cells lacking caveolae. *EMBO Rep*. 2002;3(1):95–100.
38. Foti M, et al. The neck of caveolae is a distinct plasma membrane subdomain that concentrates insulin receptors in 3T3-L1 adipocytes. *Proc Natl Acad Sci U S A*. 2007;104(4):1242–1247.
39. Kabayama K, et al. Dissociation of the insulin receptor and caveolin-1 complex by ganglioside GM3 in the state of insulin resistance. *Proc Natl Acad Sci U S A*. 2007;104(34):13678–13683.
40. Hahn-Obercyger M, et al. A high-cholesterol diet increases the association between caveolae and insulin receptors in rat liver. *J Lipid Res*. 2009;50(1):98–107.
41. Capozza F, et al. Caveolin-3 knockout mice show increased adiposity and whole body insulin resistance, with ligand-induced insulin receptor instability in skeletal muscle. *Am J Physiol Cell Physiol*. 2005;288(6):C1317–C1331.
42. Oshikawa J, et al. Insulin resistance in skeletal muscles of caveolin-3-null mice. *Proc Natl Acad Sci U S A*. 2004;101(34):12670–12675.
43. Deng YF, et al. The Caveolin-3 P104L mutation of LGMD-1C leads to disordered glucose metabolism in muscle cells. *Biochem Biophys Res Commun*. 2017;486(2):218–223.
44. Shang L, et al. The caveolin-3 P104L mutation in LGMD-1C patients inhibits non-insulin-stimulated glucose metabolism and growth but promotes myocyte proliferation. *Cell Biol Int*. 2019;43(6):669–677.
45. Huang Y, et al. Effect of type 2 diabetes mellitus caveolin-3 K15N mutation on glycometabolism. *Exp Ther Med*. 2019;18(4):2531–2539.
46. Shang L, et al. Caveolin-3 promotes glycometabolism, growth and proliferation in muscle cells. *PLoS One*. 2017;12(12):0189004.
47. Simons K, Toomre D. Lipid rafts and signal trans-

arterial smooth muscle cells. *Am J Physiol Cell Physiol*. 2012;302(2):C405–C411.
51. Ohashi K, et al. Zinc promotes proliferation and activation of myogenic cells via the PI3K/Akt and ERK signaling cascade. *Exp Cell Res*. 2015;333(2):228–237.
52. Shulman GI. Cellular mechanisms of insulin resistance. *J Clin Invest*. 2000;106(2):171–176.
53. Chavez JA, Summers SA. A ceramide-centric view of insulin resistance. *Cell Metab*. 2012;15(5):585–594.
54. Kien CL, et al. A lipidomics analysis of the relationship between dietary fatty acid composition and insulin sensitivity in young adults. *Diabetes*. 2013;62(4):1054–1063.
55. Timmers S, et al. Augmenting muscle diacylglycerol and triacylglycerol content by blocking fatty acid oxidation does not impede insulin sensitivity. *Proc Natl Acad Sci U S A*. 2012;109(29):11711–11716.
56. Demeure O, et al. Regulation of LPCAT3 by LXR. *Gene*. 2011;470(1–2):7–11.
57. Yamazaki T, et al. Peroxisome proliferators attenuate free arachidonic acid pool in the kidney through inducing lysophospholipid acyltransferases. *J Pharmacol Sci*. 2009;111(2):201–210.
58. Lyu K, et al. A membrane-bound diacylglycerol species induces PKCε-mediated hepatic insulin resistance. *Cell Metab*. 2020;32(4):654–664.
59. Heden TD, et al. Greater oxidative capacity in primary myotubes from endurance-trained women. *Med Sci Sports Exerc*. 2017;49(11):2151–2157.
60. Heden TD, et al. Mitochondrial PE potentiates respiratory enzymes to amplify skeletal muscle aerobic capacity. *Sci Adv*. 2019;5(9):eaax8352.
61. Verkerke ARP, et al. Phospholipid methylation regulates muscle metabolic rate through Ca^{2+} transport efficiency. *Nat Metab*. 2019;1(9):876–885.
62. Johnson JM, et al. Alternative splicing of UCP1 by non-cell-autonomous action of PEMT. *Mol Metab*. 2020;31:55–66.
63. Zeczycki TN, et al. Increasing levels of cardiolipin differentially influence packing of phospholipids found in the mitochondrial inner membrane. *Biochem Biophys Res Commun*. 2014;450(1):366–371.
64. Park S, et al. Electrical pulse stimulation induces differential responses in insulin action in myotubes from severely obese individuals. *J Physiol*. 2019;597(2):449–466.
65. Al-Khalili L, et al. Insulin action in cultured human skeletal muscle cells during differentiation: assessment of cell surface GLUT4 and GLUT1 content. *Cell Mol Life Sci*. 2003;60(5):991–998.
66. Holland WL, et al. Receptor-mediated activation of ceramidase activity initiates the pleiotropic actions of adiponectin. *Nat Med*. 2011;17(1):55–63.
67. Kusminski CM, et al. MitoNEET-driven alterations in adipocyte mitochondrial activity reveal a crucial adaptive process that preserves insulin sensitivity in obesity. *Nat Med*. 2012;18(10):1539–1549.
68. Sharma AX, et al. Glucagon receptor antagonism improves glucose metabolism and cardiac function by promoting AMP-mediated protein kinase in diabetic mice. *Cell Rep*. 2018;22(7):1760–1773.
69. Funai K, et al. Skeletal muscle phospholipid metabolism regulates insulin sensitivity and contractile function. *Diabetes*. 2016;65(2):358–370.
70. Funai K, et al. Muscle lipogenesis balances insulin sensitivity and strength through calcium signaling. *J Clin Invest*. 2013;123(3):1229–1240.
71. Ferrara PJ, et al. Hypothermia decreases O2 cost for ex vivo contraction in mouse skeletal muscle. *Med Sci Sports Exerc*. 2018;50(10):2015–2023.
72. Mendez J, Keys A. Density and composition of mammalian muscle. *Metabolism*. 1960;9:184–188.
73. Moorwood C, et al. Isometric and eccentric force generation assessment of skeletal muscles isolated from murine models of muscular dystrophies. *J Vis Exp*. 2013;(71):50036.
74. Brooks SV, Faulkner JA. Contractile properties of skeletal muscles from young, adult and aged mice. *J Physiol*. 1988;404:71–82.
75. Krause BR, et al. In vivo evidence that the lipid-regulating activity of the ACAT inhibitor CI-976 in rats is due to inhibition of both intestinal and liver ACAT. *J Lipid Res*. 1993;34(2):279–294.
76. Rockett BD, et al. Fish oil increases raft size and membrane order of B cells accompanied by differential effects on function. *J Lipid Res*. 2012;53(4):674–685.
77. Otsu N. A threshold selection method from gray-level histograms. *IEEE Trans Syst Man Cybern*. 1979;9(1):62–66.
78. Sezgin M, Sankur B. Survey over image thresholding techniques and quantitative performance evaluation. *J Electron Imaging*. 2004;13(1):146–168.
79. Shaikh SR, et al. Docosahexaenoic acid modifies the clustering and size of lipid rafts and the lateral organization and surface expression of MHC class I of EL4 cells. *J Nutr*. 2009;139(9):1632–1639.